Korean J. Chem. Eng., 39(8), 2127-2137 (2022)
DOI: 10.1007/s11814-022-1070-y

pISSN: 0256-1115
eISSN: 1975-7220

Metal organic frameworks template-directed fabrication of rod-like hollow $BiOCl_xBr_{1-x}$ with adjustable band gap for excellent photocatalytic activity under visible light

Ze Luo*, **Jinlong Li***,**,†, **Guozhe Sui***,**,†, **Yan Zhuang***, **Dongxuan Guo***,**, **Rongping Xu***,
Shuang Liang*, **Hong Yao***, **Chao Wang***, and **Shijie Chen***,**

*College of Chemistry and Chemical Engineering, Qiqihar University, Qiqihar 161006, P. R. China
**Heilongjiang Provincial Key Laboratory of Catalytic Synthesis for Fine Chemicals, Qiqihar University,
Qiqihar 161006, P. R. China

(*Received 22 October 2021 • Revised 22 December 2021 • Accepted 17 January 2022*)

Abstract−Developing an efficient, environmentally friendly, and pollution-free catalyst with excellent visible light catalytic activity is a promising strategy for dye wastewater treatment. Herein, the rod-like hollow $BiOCl_xBr_{1-x}$ (x=1, 0.75, 0.5, 0.25, 0), with an adjustable band gap, was successfully prepared using Bi-based metal-organic framework as template. The corresponding hollow assembly and introduction of Br^- imparted valuable structural advantages and intrinsic characteristics for improved photocatalytic activity. Significantly, the degradation efficiency of $BiOCl_{0.5}Br_{0.5}$ for the Rhodamine B (RhB) solution reached 92% under visible light illumination for 90 min, which is considerably higher than that of CAU-17-derived Bi_2O_3 and BiOCl. Overall, these findings shed fundamental insight on constructing novel photocatalysts with excellent visible light driven photocatalytic activity and offered a new method for treating dye wastewater.

Keywords: Metal-organic Frameworks, $BiOCl_xBr_{1-x}$, Hollow Structure, Photocatalysis, Visible Light

INTRODUCTION

With rapidly developing societies, water pollution related to printing, dyeing and other industries has become increasingly serious because of the potential risk to human life and health. Therefore, research on pollutant elimination has received global attention. Among the various conventional dye wastewater treatments, photocatalytic technology is considered a promising alternative due to its safe, affordable, and sustainable properties [1]. Furthermore, most reported photocatalysts are usually based on semiconductors of metal oxides and sulfides.

Bismuth oxychloride (BiOCl) is one representative semiconductor photocatalyst with desirable photocatalytic activity and stability that has spurred intense interest in treating dye wastewater [2-5]. The layered structure of BiOCl is composed of $[Bi_2O_2]^{2+}$ plates interlaced with double chlorine atoms that provide a large space for the polarization of atoms and orbitals, leading to effective electron-hole pair separation and reasonable photocatalytic activity [6]. Meanwhile, the lifespan of BiOCl electron-hole pairs is prolonged owing to their indirect transition band gap, further enhancing the photocatalytic activity. Zheng et al. [7] employed a solvothermal process to prepare BiOCl microspheres with superior photocatalytic behavior, using special morphologies and phases by regulating the ratio of ethylene glycol and N,N-dimethylformamide. The authors regulated the growth of the BiOCl nanomaterials using water as the hydrolyzing agent and ethylene glycol as the crystal growth inhibitor. The as-prepared BiOCl nanosheets with exposed (001) surfaces demonstrated favorable photocatalytic activity for degrading Rhodamine B (RhB) [8]. Wang et al. [9] successfully prepared BiOCl microflowers by employing a simple co-precipitation method, which demonstrated reasonable photocatalytic activity and stability for degrading RhB. Nevertheless, preparing BiOCl photocatalysts with a satisfactory light absorption range is complicated owing to its wide band gap. Consequently, several studies have attempted to enhance the photocatalytic activity of BiOCl by depositing noble metals [10], doping atoms [11,12], or constructing heterojunctions [13,14]. However, improving the photocatalytic activity of BiOCl remains a significant challenge.

To circumvent this drawback and widen the practical application of BiOCl, it is of great interest to construct a hollow structure combined with an adjustable band gap. Specifically, metal-organic framework (MOF) materials possess characteristics, such as high specific surface area, excellent porosity, and chemical tunability, which can provide large active sites and a stable porous structure while maintaining the overall size of the catalyst. Therefore, MOFs have not only spurred great interest as a new paradigm in material science, but have also been considered promising candidates for constructing hollow structures. Xia et al. [15] constructed hollow Co_9S_8/CdS heterostructured nanocages via a one-pot synthesis using ZIF-67 as a sacrificial template. Owing to the hollow structure, size effect of quantum dots, and abundant active sites, the separation and migration of carriers were accelerated, and the electron-hole recombination successfully suppressed; thus, the hollow Co_9S_8/CdS nanocages demonstrated remarkable activity with the hydrogen production efficiency. Similarly, bismuth-based MOFs have a wide range of applications in photocatalysis. Zhang et al. [16] converted Bi-MOF into bismuth single atom for the electrocatalytic reduction reaction of CO_2, which exhibits an unprecedented high activity

---

[†] To whom correspondence should be addressed.
E-mail: jinlong141@163.com, gzhsui@qqhru.edu.cn

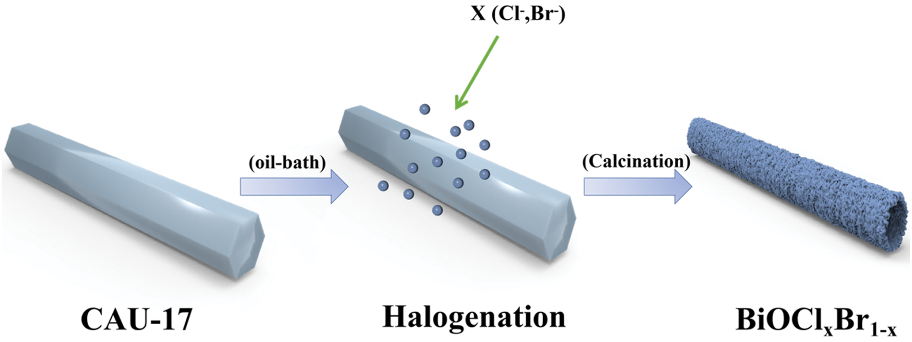

Fig. 1. Preparation scheme of $BiOCl_xBr_{1-x}$.

and selectivity.

Herein, $BiOCl_xBr_{1-x}$ rods with a hollow structure were designed and prepared using bismuth-based MOF (CAU-17) precursors. The hollow structure was intended to improve the specific surface area, provide rich active sites, enhance the absorption of visible light, and accelerate the separation of photogeneration carriers to enhance the reaction activity. Moreover, introducing Br^- with a larger radius than that of Cl^- could effectively modulate electronic structure and shorten band gap, resulting in a wide light absorption range of BiOCl. In addition, the photocatalytic activity influenced by the ratio of Cl^-/Br^- was systematically studied and explored. Consequently, $BiOCl_xBr_{1-x}$ exhibited superior photocatalytic degradation under visible light illumination. Overall, $BiOCl_xBr_{1-x}$ rods with hollow structures provide the key to unlocking the full potential of BiOCl's activity in photocatalysis.

EXPERIMENTAL

1. Chemicals

Trimesic acid (H_3BTC), methanol (MeOH), bismuth nitrate pentahydrate ($Bi(NO_3)_3·5H_2O$), ethanol (EtOH), N,N-dimethylformamide (DMF), ammonium chloride (NH_4Cl), and ammonium bromide (NH_4Br) were purchased from Aladdin Reagent Co., Ltd. Rhodamine B (RhB) was selected and dissolved as the target dye wastewater to evaluate the photocatalytic activity of the catalysts. Benzoquinone (BQ), potassium iodide (KI), and isopropanol (IPA), provided by Aladdin Reagent Co., Ltd, were used as scavengers for active groups. In this experiment, all reagents were of analytical grade and used without further purification.

2. Preparation of $BiOCl_xBr_{1-x}$

The CAU-17 was prepared following the methods reported in the literature (CAU-17) [17]. 0.75 g H_3BTC and 0.15 g $Bi(NO_3)_3·5H_2O$ were added into 60 mL MeOH and stirred to obtain the transparent solution. The reaction system was then heated to 120 °C in an oil bath under atmospheric pressure for 1 h. The resulting white powder was washed three times with MeOH, and dried in an oven at 60 °C for 12 h to obtain CAU-17.

Typically, 0.01 mol of NH_4X (X=Cl, Br) was dissolved into 50 mL of deionized water with vigorous stirring, and 0.5 g of CAU-17 mixed in the NH_4X solution using different molar ratios of NH_4Cl and NH_4Br as 1 : 0, 0.75 : 0.25, 0.5 : 0.5, 0.25 : 0.75, and 0 : 1, respectively. The resulting mixture was kept in an oil bath heating pot at 90 °C for 1 h. The resulting powder labeled as $BiOCl_xBr_{1-x}$ (x=1, 0.75, 0.5, 0.25, 0) according to the molar ratio NH_4Cl to NH_4Br was washed three times with EtOH and deionized water, and dried under vacuum at 60 °C for 12 h. $BiOCl_xBr_{1-x}$ powders were obtained after calcinating in a muffle furnace at 450 °C for 2 h with a heating rate of 1 °C·min^{-1}. For comparison, Bi_2O_3 was prepared through direct calcination without halogenation treatment.

The fabrication of $BiOCl_xBr_{1-x}$ rods with hollow structures, using the two main procedures, is schematically depicted in Fig. 1. Initially, given the high specific surface area, geometry, and periodic porosity, the rod-like CAU-17 was prepared through a facile oil bath heating method. Subsequently, CAU-17 served as the self-sacrificial template to present Bi^{3+} ions and skeletons for the later growth of $BiOCl_xBr_{1-x}$. Owing to the Kendall effect, the outward diffusion rate of Bi^{3+} is faster than the inward diffusion rate of Cl^-/Br^-, forming a hollow rod-like structure [18]. Finally, calcining treatment was performed to remove NH^{4+} and organic impurities, and the $BiOCl_xBr_{1-x}$ rods with hollow structures were prepared.

3. Characterization

X-ray diffraction (XRD) measurements were implemented by a powder X-ray diffraction system TTR-III (Rigaku, Japan) equipped with Cu Kα radiation (λ=0.15406 nm). X-ray photoelectron spectroscopy (XPS) was carried out on a Thermo ESCALAB 250Xi spectrometer (Thermo Fisher Co., America) with monochromatic Al Kα radiation (hγ=1,486.6 eV). The structure of the as-fabricated products was investigated using a field emission scanning electron microscope (FE-SEM) SU8000 (Hitachi, Japan) and transmission electron microscope (TEM) (Tecnai 12, FEI Co., America). Nitrogen adsorption-desorption experiments were carried out on an auto NOVA 2000E physisorption analyzer (Quantachrome Co., America) at 77.35 K. The thermogravimetric (TG) analysis was performed by a TG 6200 instrument (PE Co., America) using a heating rate of 10 °C·min^{-1}. The functional groups of samples were assessed by a LabRAM HR Evolution Raman spectrometer (Horiba Co., France). The photoelectrochemical measurements were acquired from a CHI 600E electrochemical workstation (Chenhua Co., China).

4. Photocatalytic Activity and Electrochemical Measurement

Taking the degradation activity of RhB (10 mg·L^{-1}) under visible light irradiation as reference, using a 500 W xenon lamp with a cut-off filter (λ>420 nm), the photocatalytic activity of the photocatalysts was tested. Additionally, 50 mL RhB solution (10 mg·L^{-1}) was mixed with 0.025 g of sample, and then stirred in the dark for

60 min to reach the absorption-desorption equilibrium. The removal efficiency of RhB was calculated from the concentration of the RhB solution measured at 15 min intervals, using the ultraviolet-visible (UV-vis) spectroscopy method after removing the photocatalysts by centrifuge. In different initial pH experiments, HCl and NaOH were employed to adjust the pH conditions of the RhB solution. The reusability of $BiOCl_xBr_{1-x}$ was determined four times by cyclic photocatalytic experiment, after repeated centrifuging and washing with ethanol. In the active species capture experiment, IPA (10 mM), KI (6 mM), and BQ (6 mM) were used to remove hydroxyl radicals (•OH), holes (h^+), and superoxide anion radicals (•O_2^-), respectively.

Electrocatalytic activity measurements were performed in a standard three-electrode mode, where a Pt foil acted as the counter electrode and Ag/AgCl as the reference electrode. The as-synthesized slurry containing 3 mg $BiOCl_xBr_{1-x}$ in 0.5 mL DMF was coated onto FTO by applying a suitable compressive force to prepare the working electrode. The electrode was made by heating at 100 °C for 30 min.

RESULTS AND DISCUSSION

1. Characterization

XRD analysis is an efficient technique to confirm the phase information of the products, and the corresponding results of the samples are shown in Fig. 2(a). A series of typical MOF peaks were observed in CAU-17 [17]. After the crystallizing process between CAU-17 and Cl^-/Br^-, the typical peaks of CAU-17 vanished with a concomitant emergence of new peaks, attributed to the formation of new products [19]. Furthermore, the diffraction peaks of $BiOCl_xBr_{1-x}$ shifted to a smaller angle zone with increasing content of Br^- in $BiOCl_xBr_{1-x}$, owing to the smaller ionic radius of Cl^- (1.81 Å) than Br^- (1.95 Å) [20]. Moreover, the XRD pattern of the calcinated CAU-17 corresponded with the standard peaks of Bi_2O_3, whereas the peaks of the organic ligands in CAU-17 completely disappeared. Therefore, the organic structure in CAU-17 was completely removed during the calcination process, and the bismuth center in the framework was transformed into the Bi_2O_3 phase during the oxidation process [21]. Meanwhile, the degree of tensile strain on the (101) face of the samples was calculated according to the XRD data, and the results are presented in Table 1. The degree of tensile strain of the crystal lattice increases with increasing Br^- content, and $BiOCl_{0.5}Br_{0.5}$ yields the most desirable photocatalytic properties at a tensile strain of 1.8%.

Raman spectra of the photocatalysts are shown in Fig. 2(b). As for BiOCl, the peak located at 147 cm^{-1} corresponds to the A_{1g} internal Bi-Cl stretching mode, whereas the peak situated at 203 cm^{-1} is the E_g internal Bi-Cl stretching mode [22]. Furthermore, the distinct vibrational band centered at 115 cm^{-1} in BiOBr is attributed to the A_{1g} internal Bi-Br stretching mode [23]. When the doping element enters into the crystal lattice, subtle changes in the crystal lattice structure can cause the shift of Raman spectrum peaks and the full width at half maxima (FWHM) variation. According to the previous literature, the F2g mode shift qualitatively follows a shift of the lattice stretching peak towards lower wavenumbers (red shift) and the lattice contraction peak towards higher wavenumbers (blue shift) [24]. As the Br^- doping increases, the mode shifts to a lower angle (red-shift), further confirming the lattice tensile strain generated by $BiOCl_xBr_{1-x}$, corresponding with the XRD results [25].

SEM and TEM images of CAU-17 and $BiOCl_xBr_{1-x}$ were systematically determined and the results are shown in Fig. 3. The SEM images revealed that CAU-17, with a uniform rod-like shape and smooth surface, was successfully prepared (Fig. 3(a)-(c)). The CAU-17 was subsequently converted into the BiOCl, $BiOCl_{0.5}Br_{0.5}$, and BiOBr intermediates without any obvious fractures after reacting with NH_4Cl or NH_4Br, and the surfaces became fine flower-

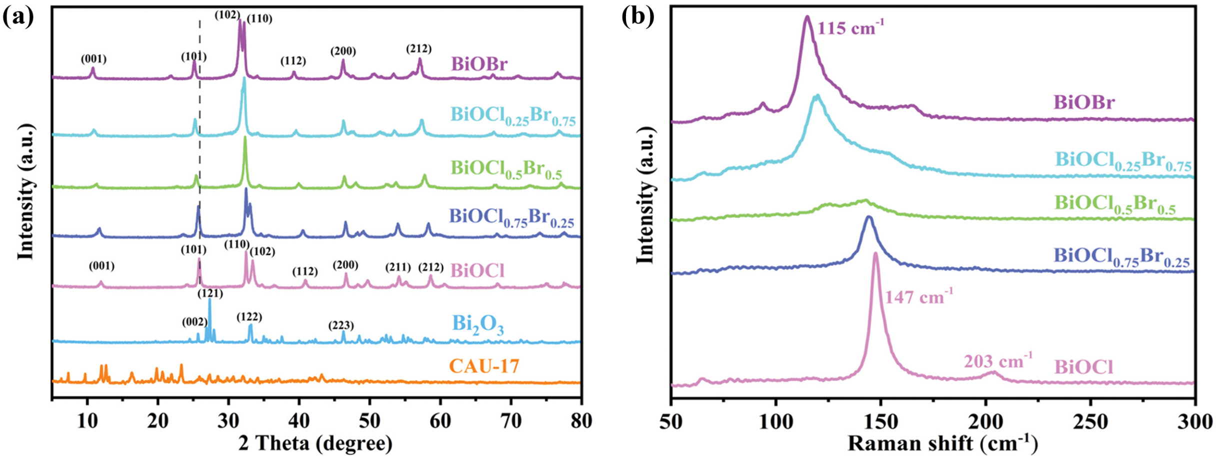

Fig. 2. (a) XRD patterns of synthesized photocatalysts, and (b) Raman spectra of $BiOCl_xBr_{1-x}$.

Table 1. Degree of lattice tensile strain of $BiOCl_xBr_{1-x}$

$BiOCl_xBr_{1-x}$	BiOCl	$BiOCl_{0.75}Br_{0.25}$	$BiOCl_{0.5}Br_{0.5}$	$BiOCl_{0.25}Br_{0.75}$	BiOBr
Degree of lattice tensile strain (%)	0	0.54	1.8	2.35	0

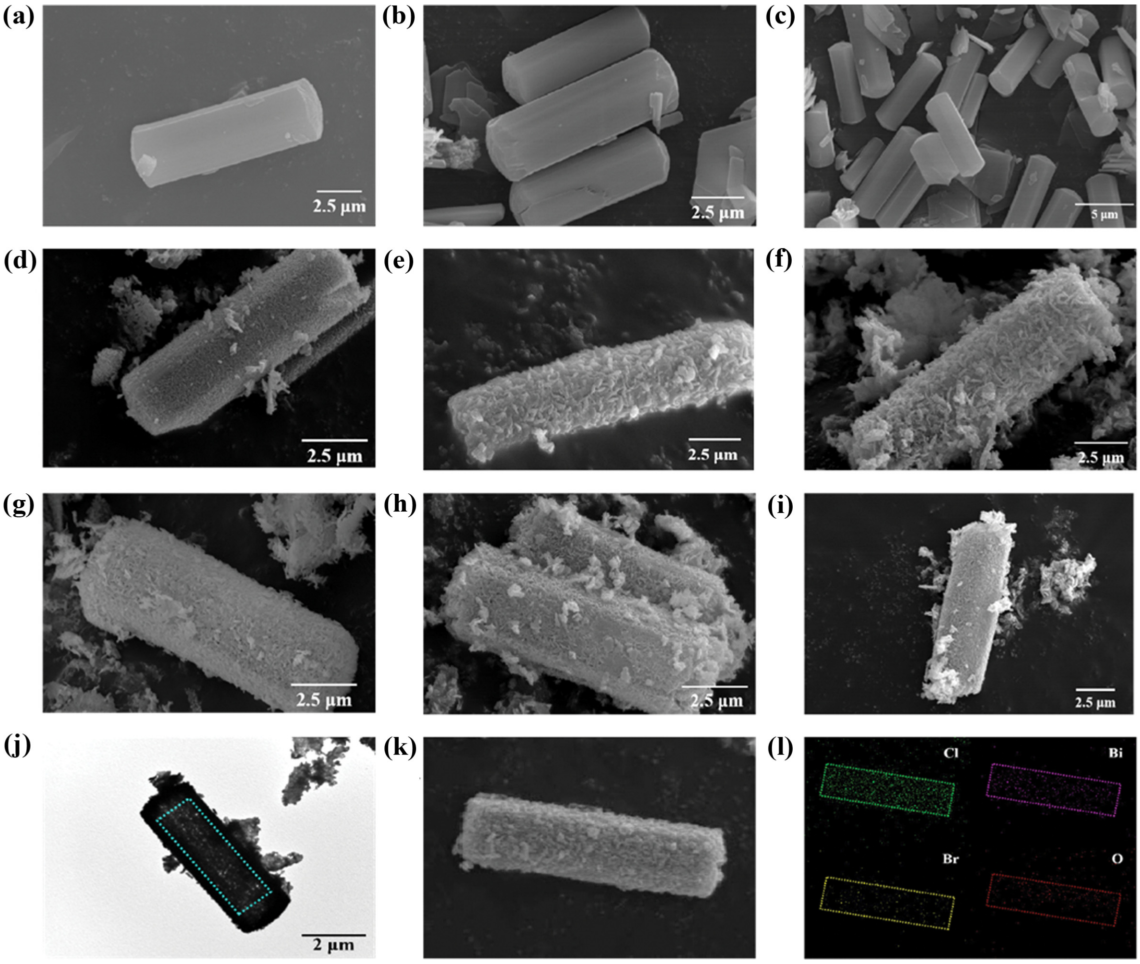

Fig. 3. The SEM images of (a)-(c) CAU-17, (d) BiOCl intermediate, (e) $BiOCl_{0.5}Br_{0.5}$ intermediate, (f) BiOBr intermediate, (g) BiOCl, (h) $BiOCl_{0.5}Br_{0.5}$, (i) BiOBr, and the TEM images of (j) $BiOCl_{0.5}Br_{0.5}$, and SEM image (k) and EDS mapping images (l) for $BiOCl_{0.5}Br_{0.5}$.

Table 2. The mass content of elements in the $BiOCl_xBr_{1-x}$

Sample	Mass content (wt%)				Theoretical molar ratio of Cl/Br	Actual molar ratio of Cl/Br
	Bi	O	Cl	Br		
$BiOCl_{0.75}Br_{0.25}$	73.005	6.061	11.49	9.444	3 : 1	2.74 : 1
$BiOCl_{0.5}Br_{0.5}$	71.456	5.759	6.222	16.563	1 : 1	1 : 1.18
$BiOCl_{0.25}Br_{0.75}$	71.859	6.128	2.536	19.477	1 : 3	1 : 3.41

like shapes having a greater surface area (Fig. 3(d)-(f)). After calcination, BiOCl, $BiOCl_{0.5}Br_{0.5}$, and BiOBr retained the rod-like shape with a diameter of 2-3 μm as the same of CAU-17 precursors (Fig. 3(g)-(i)). Notably, $BiOCl_{0.5}Br_{0.5}$ had a hollow/porous structure because of the diffusion-controlled process under mild reaction conditions, as shown in Fig. 3(j). Furthermore, the energy dispersive spectroscopy (EDS) mapping image of $BiOCl_{0.5}Br_{0.5}$ is presented in Fig. 3(k)-(l), and the Bi, O, Cl, and Br elements are evenly distributed over the surface of the rod, indicating a homogeneous phase structure of the sample. The mass content of elements in the $BiOCl_xBr_{1-x}$ was determined by EDS analysis as shown in Table 2, indicating that the actual molar ratio of Cl/Br was basically consistent with the theoretical value. Importantly, the hollow structure and flower-like surface could improve the specific surface area and rich active sites, which accelerates the separation of carriers and enhances the reaction activity [26].

XPS was adopted to analyze the composition of $BiOCl_{0.5}Br_{0.5}$, and the spectra are illustrated in Fig. 4. The Bi, O, Cl, and Br elements are uniformly distributed on $BiOCl_{0.5}Br_{0.5}$ (Fig. 4(a)). In addition, two typical peaks situated at 164.2 and 158.8 eV are assigned to Bi $4f_{5/2}$ and Bi $4f_{7/2}$ (Fig. 4(b)), respectively, confirming the existence of Bi^{3+}. Fig. 4(c) shows the O 1s spectrum, which depicts three peaks at 532.6, 531.0, and 528.8 eV, assigned to the O-H, $O_{(V)}$, and Bi-O bonds, respectively [27]. The two peaks of Cl 2p situated at 199.5 and 197.8 eV in Fig. 4(d) are attributed to Cl $2p_{1/2}$ and Cl $2p_{3/2}$, respectively. Finally, the two peaks centered at 69.0 and 68.0

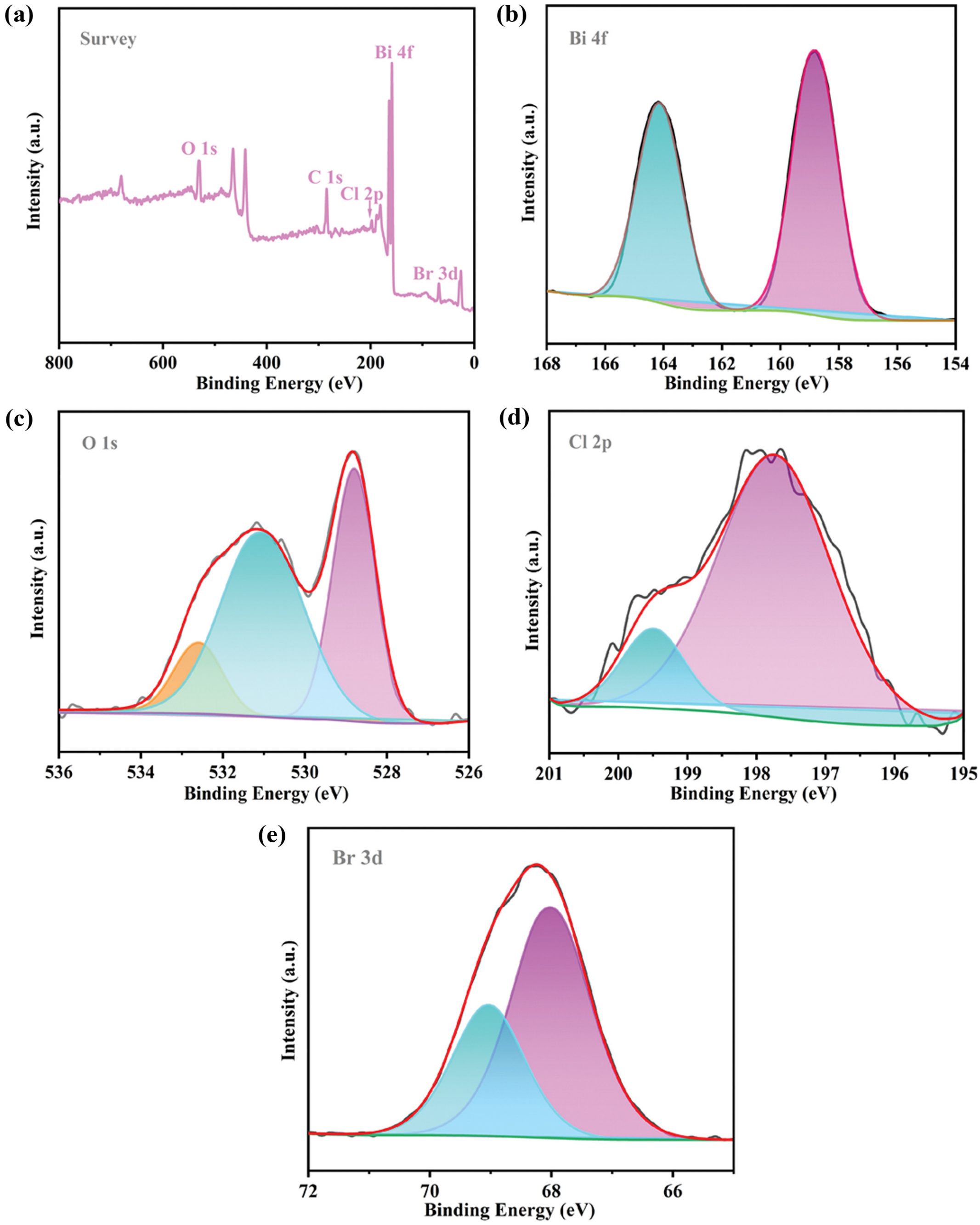

Fig. 4. XPS spectra of BiOCl$_{0.5}$Br$_{0.5}$: (a) survey, (b) Bi 4, (c) O1s, (d) Cl 2p, (e) Br 3d.

eV belong to Br 3d$_{3/2}$ and Br 3d$_{5/2}$, respectively (Fig. 4(e)) [28]. The XPS results confirm that BiOCl$_{0.5}$Br$_{0.5}$ was successfully prepared [29].

The diffuse reflectance spectra (DRS) of all samples are shown in Fig. 5(a). The absorption boundaries of BiOCl, BiOCl$_{0.75}$Br$_{0.25}$, BiOCl$_{0.5}$Br$_{0.5}$, BiOCl$_{0.25}$Br$_{0.75}$, and BiOBr are positioned at approximately 385, 417, 425, 433, and 444 nm, respectively. Compared to BiOCl, BiOCl$_x$Br$_{1-x}$ exhibits a wider range of light absorption from UV to visible light with increasing Br$^-$ [30]. The transformed Kubelka-Munk plots as a function of light energy are shown in Fig. 5(b). The estimated band gap energy (Eg value) of BiOCl, BiOCl$_{0.75}$Br$_{0.25}$, BiOCl$_{0.5}$Br$_{0.5}$, BiOCl$_{0.25}$Br$_{0.75}$, and BiOBr is 3.00, 2.77, 2.73, 2.69 and 2.65 eV, respectively. This shows that the Eg values of BiOCl$_x$Br$_{1-x}$ decreased with increasing Br$^-$ [31]. The VB position consists of Bi 6s, O 2p, Cl 3p, and Br 4p orbitals, while the CB position consists of Bi 6s and Bi 6p orbitals. Therefore, the VB position can be adjusted by changing the ratio of the Cl 3p and Br 4p orbitals, and the CB position can be changed accordingly. A wide spectrum of light absorption is obtained by adjusting the Cl/Br ratio to appropriately narrow the band gap. Although the light absorption range could be broadened by narrowing the band gap, this usually inhibits the oxidation ability. Therefore, the Eg values can be reasonably adjusted by controlling the molar ratio of Cl$^-$/Br$^-$. According to the

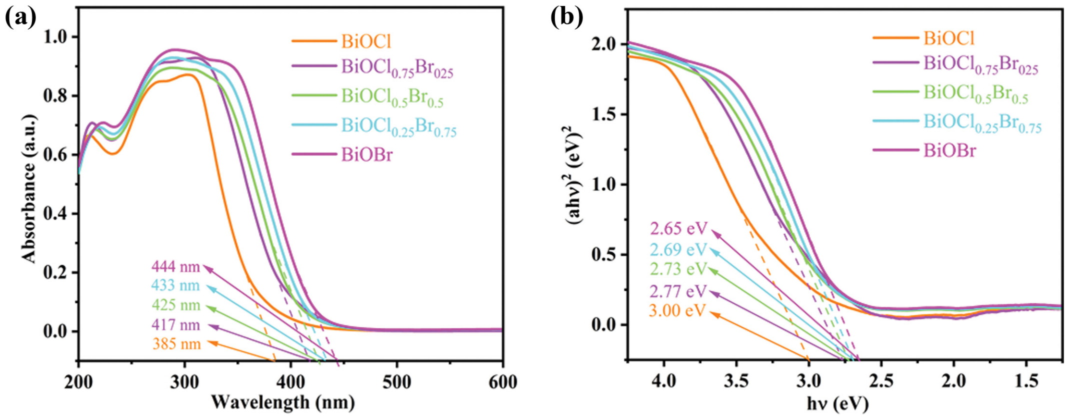

Fig. 5. (a) UV-vis DRS spectra, and (b) plots of transformed Kubelka-Munk function versus the energy of light for all samples.

Table 3. Absorption edge, calculated optical band gaps, conduction band bottoms (CB), and valence band tops (VB) of BiOCl$_x$Br$_{1-x}$

BiOCl$_x$Br$_{1-x}$	BiOCl	BiOCl$_{0.75}$Br$_{0.25}$	BiOCl$_{0.5}$Br$_{0.5}$	BiOCl$_{0.25}$Br$_{0.75}$	BiOBr
Absorption edge (nm)	385	417	425	433	444
Optical band gap (eV)	3.00	2.77	2.73	2.69	2.65
CB potential (eV)	−0.49	−0.37	−0.35	−0.33	−0.37
VB potential (eV)	2.52	2.40	2.38	2.36	2.28

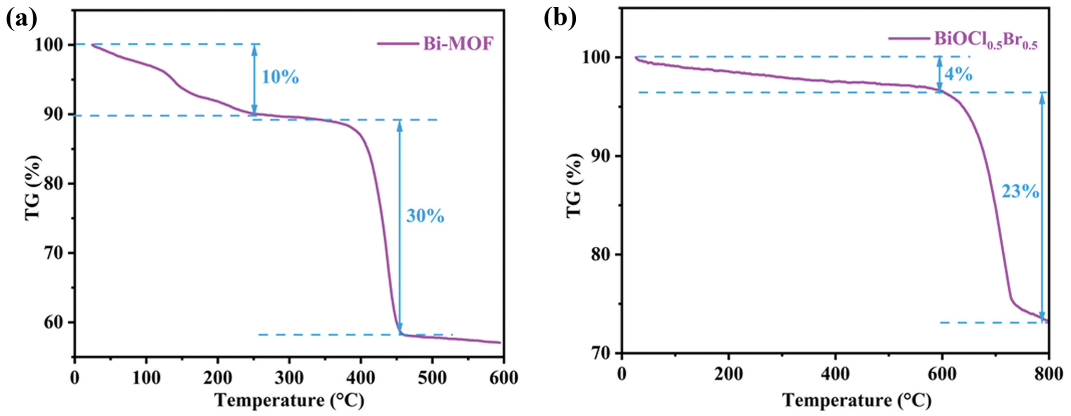

Fig. 6. Thermogravimetry of (a) Bi-MOF, and (b) BiOCl$_{0.5}$Br$_{0.5}$.

above data, the relative conduction band (CB) and valence band (VB) positions of BiOCl$_x$Br$_{1-x}$ with different x values were estimated, as shown in Table 3 [32].

The thermal stability of CAU-17 and BiOCl$_{0.5}$Br$_{0.5}$ were analyzed by TG curves, as shown in Fig. 6(a) and (b). The 10% mass change in precursor CAU-17 below 250 °C is attributed to the loss of water and ethanol molecules, whereas the 30 wt% mass change in the 350-450 °C range corresponds to the conversion of CAU-17 to Bi_2O_3 (Fig. 6(a)) [33]. As shown in Fig. 6(b), BiOCl$_{0.5}$Br$_{0.5}$ has a mass loss of approximately 4 wt% in the 0-600 °C range owing to the absorbed and crystal water. By comparison, the significant weight loss (23 wt%) above 600 °C indicates a change in the crystal structure of BiOCl$_{0.5}$Br$_{0.5}$. Therefore, BiOCl$_{0.5}$Br$_{0.5}$ possessed excellent thermal stability below 600 °C [34,35].

The degradation behavior of photocatalysts is closely related to the specific surface area. In general, photocatalysts having a high specific surface area can readily absorb and migrate target reactants through porous structures, thereby significantly improving the degradation efficiency due to the presence of rich active sites. N_2 adsorption-desorption isotherms of BiOCl$_x$Br$_{1-x}$ are shown in Fig. 7(a), and the corresponding pore size distribution is shown in Fig. 7(b). According to the IUPAC classification, the N_2 adsorption-desorption curve of BiOCl$_x$Br$_{1-x}$ is considered a type IV isotherm with clear hysteresis loops (Fig. 7(a)), indicating that a mesoporous structure existed in BiOCl$_{0.5}$Br$_{0.5}$. Furthermore, the tails of these isotherms revealed an upward tendency at the relative pressure of 1, which suggests the existence of macropores. Moreover, BiOCl$_{0.5}$Br$_{0.5}$ acquires a relatively large Brunauer-Emmet-Teller (BET) specific surface area of 27.83 $cm^2{\cdot}g^{-1}$ compared with 36.12 $cm^2{\cdot}g^{-1}$, 30.26 $cm^2{\cdot}g^{-1}$, 14.87 $cm^2{\cdot}g^{-1}$, and 12.98 $cm^2{\cdot}g^{-1}$ of BiOCl, BiOCl$_{0.75}$Br$_{0.25}$, BiOCl$_{0.25}$Br$_{0.75}$, and BiOBr. The pore size distribution of the samples further confirms the existence of mesoporous structure as

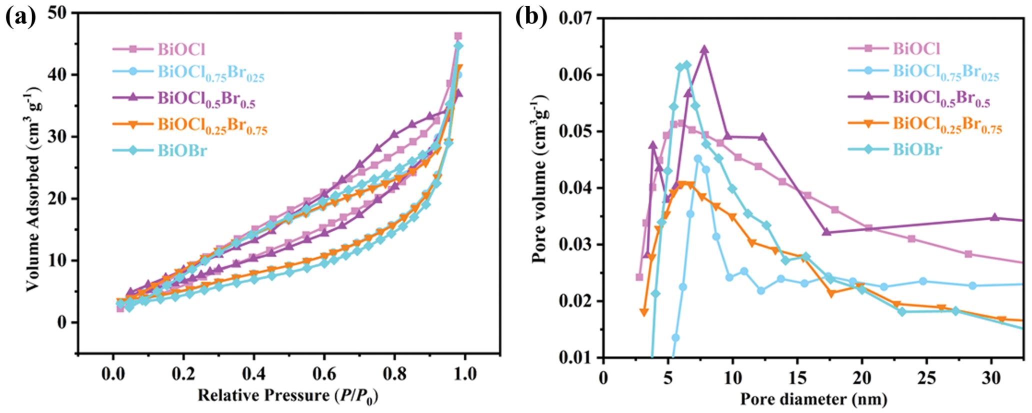

Fig. 7. (a) Nitrogen adsorption/desorption and (b) pore size distributions of BiOCl$_x$Br$_{1-x}$.

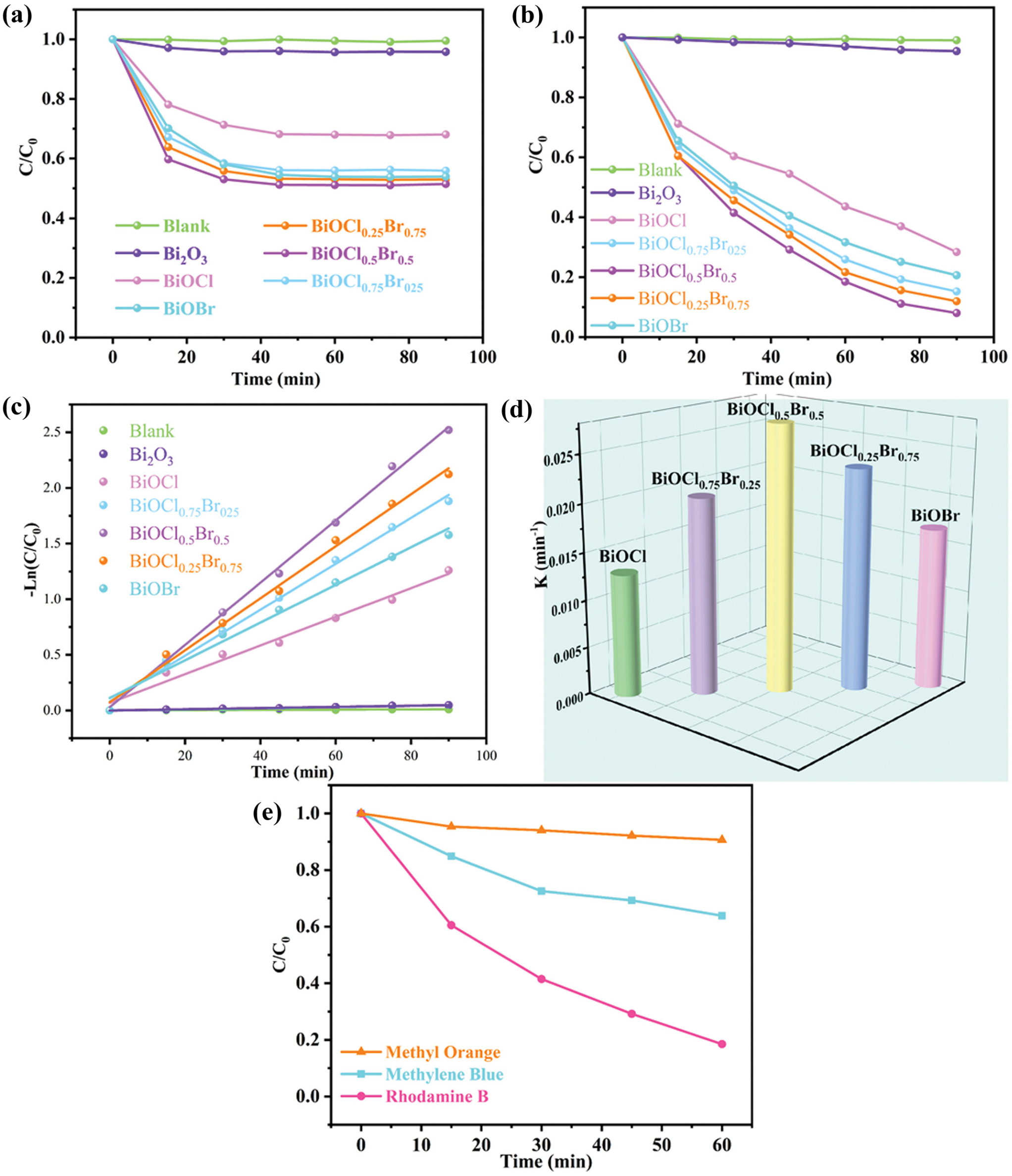

Fig. 8. (a) Adsorption curves of synthesized photocatalysts on RhB in dark, (b) photocatalytic activity of synthesized photocatalysts for RhB degradation, (c) kinetic linear simulation curves, (d) kinetic constants of synthesized photocatalysts for RhB degradation, and (e) photocatalytic activity of BiOCl$_{0.5}$Br$_{0.5}$ for degraded RhB, MB, and MO dyes.

depicted in Fig. 7(b). Therefore, the large specific surface area contributes to the establishment of a synergistic adsorption-degradation system, which is one of the main reasons for the enhancement of photodegradation performance [36,37].

2. Photocatalytic Activity and Mechanism

To investigate the photocatalytic activity of the samples, aqueous RhB (10 mg·L^{-1}) was selected as the simulated dye wastewater under visible light illumination. All samples were adsorbed in the dark for 60 min to reach the equilibrium of adsorption-desorption as shown in Fig. 8(a). In addition, the possible degradation by direct photolysis (without photocatalyst) was also investigated and the results of experiment are shown in Fig. 8(b). Almost no concentration change of RhB was observed without any photocatalysts, while RhB degraded gradually with the presence of photocatalysts. Comparing the photocatalytic activity of Bi_2O_3, BiOCl, $BiOCl_{0.75}Br_{0.25}$, $BiOCl_{0.5}Br_{0.5}$, $BiOCl_{0.25}Br_{0.75}$, and BiOBr, $BiOCl_{0.5}Br_{0.5}$ samples exhibited much higher photocatalytic activity. The degradation efficiency of $BiOCl_{0.5}Br_{0.5}$ for the RhB solution reached 92% under visible light illumination for 90 min, which was significantly higher than that of BiOCl (72%), Bi_2O_3 (5%), $BiOCl_{0.75}Br_{0.25}$ (85%), $BiOCl_{0.25}Br_{0.75}$ (88%), and BiOBr (79%) [38]. As shown in Fig. 8(c) and (d), the kinetic constants (k) of different catalysts for removing RhB in dye wastewater were calculated, and the photocatalytic reaction followed a first-order dynamic model. The k value of $BiOCl_{0.5}Br_{0.5}$ is approximately 2.2, 1.4, 1.2, and 1.6 times that of BiOCl, $BiOCl_{0.75}Br_{0.25}$, $BiOCl_{0.25}Br_{0.75}$, and BiOBr, respectively. To thoroughly evaluate the photocatalytic activity of $BiOCl_{0.5}Br_{0.5}$, Methylene Blue (MB) and Methyl Orange (MO) were selected as simulated pollutants in addition to RhB. With the decreasing molar ratio of Cl/Br, the photocatalytic activity of $BiOCl_xBr_{1-x}$ (x=0.75, 0.5) for the degradation of RhB increased. This result can be ascribed to the doping of Br^-, which leads to narrower band gap and lattice strain, and thus resulting in structural defects such as vacancies. The narrower band gap enhances the utilization of light energy and the resultant defects can act as trapping centers to inhibit the recombination of photogenerated electron-holes. However, when the molar ratio of Cl/Br exceeds 1 : 1, the rate of charge recombination will increase due to the too small distance between separating electron and hole, resulting in a decreased number of effective charge carriers [39]. From Fig. 8(e), the degradation efficiency of RhB was higher than those of MB and MO, considering the difficulty degrading the symmetric structures of MB and MO.

The influence of the initial solution pH on the photocatalytic degradation efficiency of RhB without and with $BiOCl_{0.5}Br_{0.5}$ was investigated, and the results are shown in Fig. 9. As shown in the Fig. 9(a), the degradation efficiency of RhB varies in the range of 2%, indicating that pH value has a weak effect on RhB without $BiOCl_{0.5}Br_{0.5}$. Decreasing the initial solution pH increased the photocatalytic activity of $BiOCl_{0.5}Br_{0.5}$ for removing RhB. RhB is considered as an organic dye with weak and moderately basic sites

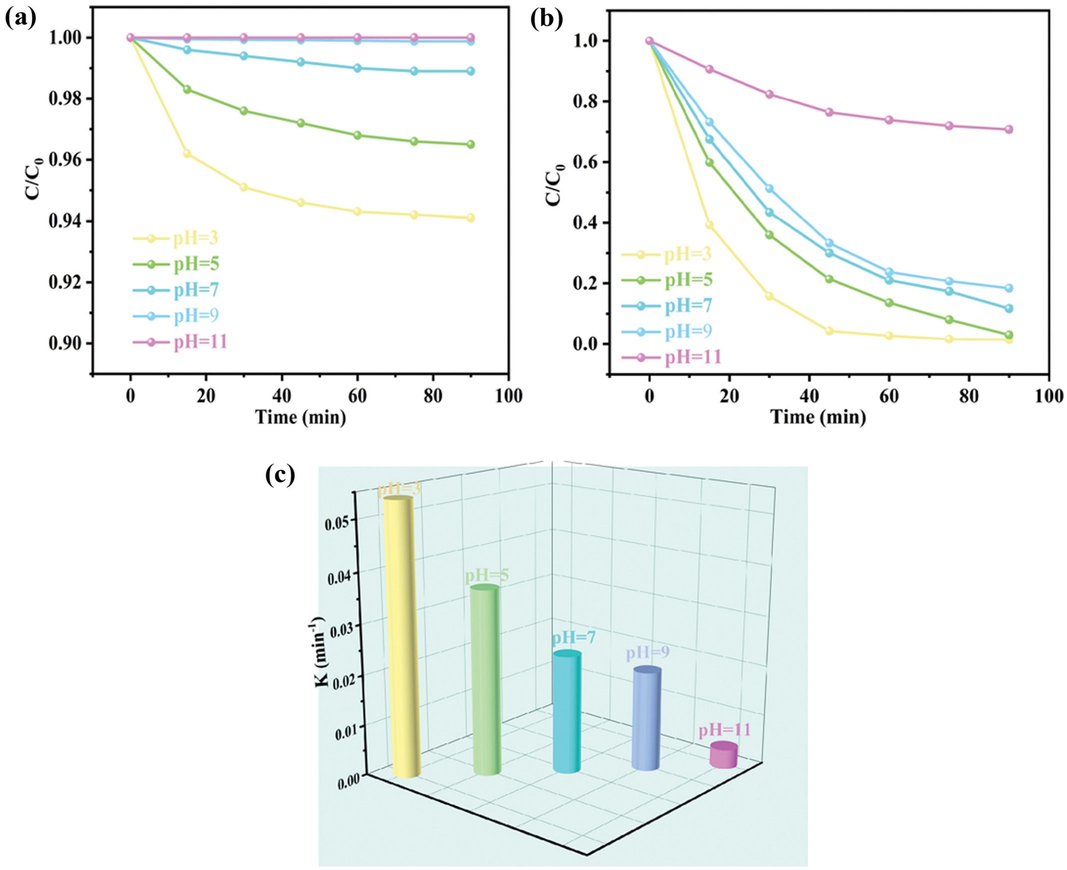

Fig. 9. (a) Photocatalytic degradation efficiency of RhB without $BiOCl_{0.5}Br_{0.5}$, (b) photocatalytic degradation efficiency of RhB with $BiOCl_{0.5}Br_{0.5}$, and (c) kinetic constants of $BiOCl_{0.5}Br_{0.5}$ under different initial pH values.

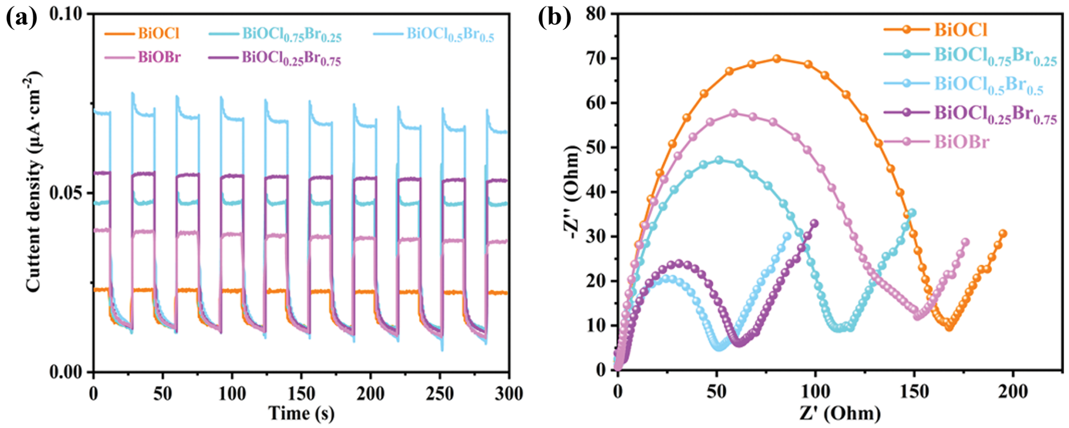

Fig. 10. (a) Transient photogenerated current spectra, and (b) EIS spectra of different photocatalysts.

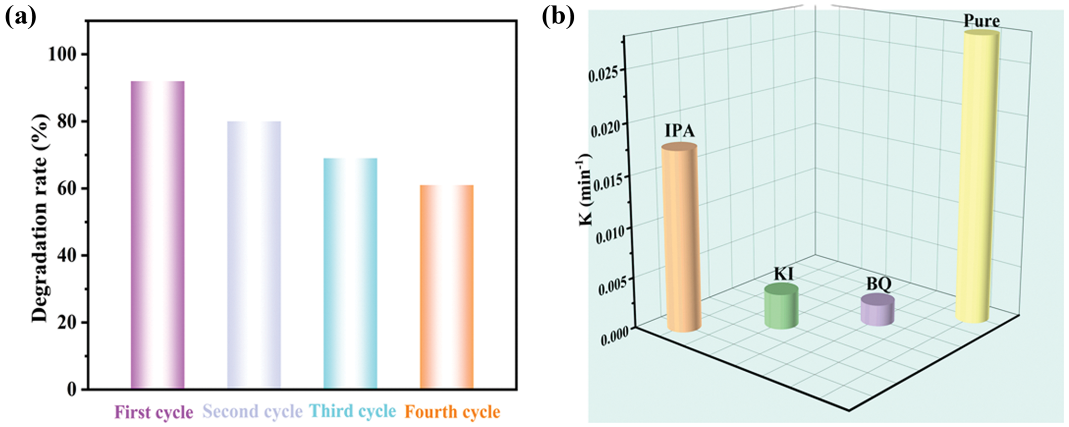

Fig. 11. (a) Cycling experiment, and (b) kinetic constants of radicals quenching experiments of $BiOCl_{0.5}Br_{0.5}$ in the photocatalytic degradation of RhB.

and therefore readily interacts with $BiOCl_{0.5}Br_{0.5}$ photocatalyst in acid solution. Overall, $BiOCl_{0.5}Br_{0.5}$ delivers desirable RhB degradation efficiency in acidic solutions [40].

The transient photocurrent test of the intermittent optical switch is considered as an effective technique for estimating the light-excited carrier separation capability. As shown in Fig. 10(a), the photocurrent of all samples varies considerably when the light is switched on and off, indicating the decent photo-response of the $BiOCl_xBr_{1-x}$. In addition, impedance spectroscopy is considered as a suitable indicator of charge carrier migration and interface transfer/recombination rate. Meanwhile, the $BiOCl_{0.5}Br_{0.5}$ shows the highest photocurrent response of 0.078 $\mu A \cdot cm^{-2}$, which is approximately 3.4, 1.5, 1.4 and 2.0 times than that of BiOCl, $BiOCl_{0.75}Br_{0.25}$, $BiOCl_{0.25}Br_{0.75}$ and BiOBr, respectively. $BiOCl_{0.5}Br_{0.5}$ exhibits the best charge separation efficiency and longest lifetime of photoinduced charge carriers, which is consistent with the photocatalytic degradation activity of RhB [41]. Fig. 10(b) delivers the impedance spectra of different samples under similar light conditions. Curves with a large radius indicate high charge transfer resistance and low transfer reaction kinetics. $BiOCl_{0.75}Br_{0.25}$, $BiOCl_{0.5}Br_{0.5}$, and $BiOCl_{0.25}Br_{0.75}$ samples show a smaller radius than BiOCl and BiOBr, where $BiOCl_{0.5}Br_{0.5}$ demonstrates the smallest radius among the five samples, indicating the best electrical conductivity and a faster charge transfer efficiency. This is attributed to the introduction of Br^-, which results in higher charge mobility at the interface. Therefore, the above results suggest that the as-prepared $BiOCl_xBr_{1-x}$ facilitates charge separation and migration efficiency, resulting in enhanced photocatalytic activity [42].

The cycling performance of $BiOCl_{0.5}Br_{0.5}$ for degrading RhB was investigated and the results are shown in Fig. 11(a). A high retention of photocatalytic activity is maintained after four cycles, indicating that the $BiOCl_{0.5}Br_{0.5}$ catalyst exhibits favorable reusability, which confirms the utility of $BiOCl_{0.5}Br_{0.5}$ in the field of dye wastewater treatment. Radical quenching experiments were engaged to investigate the active species contributing to the photodegradation of RhB in this system. KI, IPA, and BQ were selected as scavenging agents for photogenerated holes (h^+), hydroxyl radicals (•OH), and superoxide radicals ($\bullet O_2^-$), respectively, and the results are shown in Fig. 11(b). Compared to the blank experiment, addition of KI and BQ inhibited the degradation rate of RhB by $BiOCl_{0.5}Br_{0.5}$ under visible light illumination. Thus, h^+ and $\bullet O_2^-$ were identified as the most important active species in $BiOCl_{0.5}Br_{0.5}$ for the photocatalytic degradation of RhB [43,44].

The CB and VB of $BiOCl_xBr_{1-x}$ were calculated and the photo-

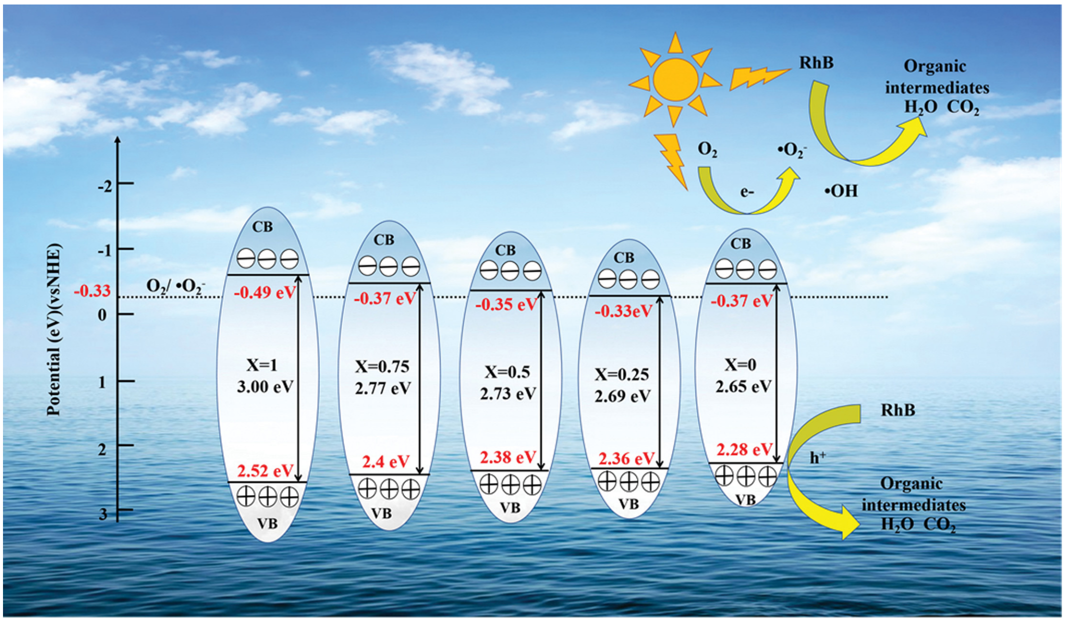

Fig. 12. Photocatalytic degradation mechanism of $BiOCl_xBr_{1-x}$ for RhB degradation.

degradation mechanism of $BiOCl_xBr_{1-x}$ for RhB was investigated, as shown in Fig. 12. The VB and CB position can be adjusted by changing the ratio of the Cl 3p and Br 4p orbitals. Therefore, $BiOCl_xBr_{1-x}$ with a narrow band gap will widen the spectrum range of light absorption to utilize the light energy [45]. Based on the DRS analysis, $BiOCl_xBr_{1-x}$ broadens the visible light response range and acquires a suitable band gap width (2.73 eV), which enhances the utilization of light energy. Meanwhile, the defects caused by the doping of Br^- will serve as trap centers for trapping photogenerated electrons, and prolonging the recombination of photogenerated electrons and holes [45]. Combined with the radical quenching experiment, h^+ and O_2^- are demonstrated as the mainly active group during the photodegradation procedure. Under visible light irradiation, the electrons leap from VB to CB in $BiOCl_xBr_{1-x}$ to form photogenerated electrons, while the photogenerated holes (h^+) remain in VB. h^+ can react with RhB molecules directly. However, h^+ generated in VB could react with OH^- to offer •OH by comparing the standard redox potentials of possible reactions because the VB edge potential of $BiOCl_xBr_{1-x}$ is higher than that of $\bullet OH/OH^-$ (+1.99 eV vs. NHE) for the standard redox potential [46]. The photogenerated electrons in CB react with O_2 molecule in water to form $\bullet O_2^-$ because the reduction potential for this reaction is −0.33 eV, which is considerably lower than the CB potential (−1.17 eV) [47]. Except that $\bullet O_2^-$ can react directly with RhB molecules, $\bullet O_2^-$ reacts with e^- and H^+ to generate H_2O_2 (0.87 eV) which reacts with e^- to generate •OH (1 eV) [48]. •OH produced by two ways can also contribute to the degradation process. Finally, the RhB molecules adsorbed on the surface are oxidized to other organic intermediates H_2O and CO_2 through the combined reaction of $\bullet O_2^-$, h^+, and •OH [49]. The possible degradation process can be written as the following equations:

$$BiOCl_xBr_{1-x}+\text{visible light}\rightarrow h^++e^- \tag{1}$$

$$O_2+e^-\rightarrow \bullet O_2^- \tag{2}$$

$$\bullet O_2^-+e^-+2H^+\rightarrow H_2O_2 \tag{3}$$

$$H_2O_2+e^-\rightarrow OH^-+\bullet OH \tag{4}$$

$$h^++OH^-\rightarrow \bullet OH \tag{5}$$

$$\bullet RhB^++h^+ \text{ or } \bullet O_2^- \text{ or } \bullet OH\rightarrow \text{degradation products} \tag{6}$$

The energy band structure of semiconductor catalysts has a crucial influence on their photocatalytic activity. Although the light absorption range could be broadened by narrowing the band gap, this usually inhibits the oxidation ability; therefore, tuning the electronic structure to achieve an optimal balance between light absorption and oxidation ability is essential to improve the photocatalytic activity of $BiOCl_xBr_{1-x}$ samples [50,51].

CONCLUSION

Bismuth-based metal-organic frameworks were used for the successful fabrication of rod-like hollow $BiOCl_xBr_{1-x}$ catalysts with an adjustable band gap. The as-prepared $BiOCl_{0.5}Br_{0.5}$ had a relatively high specific surface area and retained the special structure of CAU-17, which provided additional active sites. Furthermore, introducing Br^- shortened the band gap of BiOCl. Under the synergistic effects of the structure and composition of the photocatalyst, $BiOCl_{0.5}Br_{0.5}$ exhibited superior photocatalytic degradation efficiency of a RhB solution under visible light illumination, compared to CAU-17-derived Bi_2O_3 and BiOCl. Overall, this work demonstrates new opportunities for developing high-performance semiconductor photocatalysts with excellent photocatalytic activity under visible light.

ACKNOWLEDGEMENTS

This work was supported by the Research Project of Education Ministry of Heilongjiang Province of China (135409101, 135409401).

CONFLICT OF INTEREST

There is no conflict of interest.

REFERENCES

1. G. Z. Sui, J. L. Li, L. J. Du, Y. Zhuang, Y. L. Zhang, Y. F. Zou and B. X. Li, *J. Alloy. Compd.*, **283**, 153851 (2020).
2. S. O. Zhao, Y. W. Zhang, Y. M. Zhou, C. Zhang, X. L. Sheng, J. S. Fang and M. Y. Zhang, *ACS Sustain. Chem. Eng.*, **5**, 1416 (2017).
3. J. L. Li, L. J. Du, S. Q. Jia, G. Z. Sui, Y. L. Zhang, Y. Zhuang, B. X. Li and Z. Y. Xing, *RSC Adv.*, **8**, 29654 (2018).
4. Y. He, J. Y. Li, K. L. Li, M. L. Sun, C. W. Yuan, R. M. Chen, J. P. Sheng, G. Leng and F. Dong, *Chinese J. Catal.*, **41**, 1430 (2020).
5. S. Yin, J. Di, M. Li, W. M. Fan, J. X. Xia, H. Xu, Y. L. Sun and H. M. Li, *Clean-Soil Air Water*, **44**, 781 (2016).
6. G. Liu, T. Wang, S. Ouyang, L. Liu, H. Jiang, Q. Yu, T. Kako and J. Ye, *J. Mater. Chem. A*, **3**, 8123 (2015).
7. Y. Zheng, X. Hu, C. M. Wu, M. X. Chen, Q. F. Chen, Y. Wang, S. Hu, J. Xiang, Q. Liu, X. Zhang and P. Yang, *J. Phys. Chem. Solids*, **135**, 109119 (2019).
8. X. Zhang, X. B. Wang, L. W. Wang, W. K. Wang, L. L. Long, W. W. Li and H. Q. Yu, *ACS Appl. Mater. Inter.*, **6**, 7766 (2014).
9. J. H. Wang and Z. M. Zhang, *Optik*, **204**, 164149 (2020).
10. D. O. Adenuga, S. M. Tichapondwa and E. M. N. Chirwa, *J. Photoch. Photobio. A*, **401**, 112747 (2020).
11. C. L. Yu, H. B. He, Q. Z. Fan, W. Y. Xie, Z. Liu and H. B. Ji, *Sci. Total Environ.*, **694**, 133727 (2019).
12. H. Maimaitizi, A. Abulizi, K. Kadeer, D. Talifu and Y. Tursun, *Appl. Surf. Sci.*, **502**, 144083 (2020).
13. X. Gao, Y. Feng, P. Y. Dong, B. B. Zhang, T. Chen, X. W. Chen, C. Liu, X. G. Xi and Z. G. Zou, *Appl. Surf. Sci.*, **521**, 146334 (2020).
14. J. L. Li, S. Q. Jia, G. Z. Sui, L. J. Du and B. X. Li, *RSC Adv.*, **7**, 34857 (2017).
15. C. Xia, C. Y. Xue, W. X. Bian, J. Liu, J. J. Wang, Y. J. Wei and J. B. Zhang, *ACS Appl. Nano Mater.*, **4**, 2743 (2021).
16. E. H. Zhang, T. Wang, K. Yu, J. Liu, W. X. Chen, A. Li, H. P. Rong, R. Lin, S. F. Ji, X. S. Zhene, Y. Wang, L. R. Zheng, C. Chen, D. S. Wang, J. T. Zhang and Y. D. Li, *J. Am. Chem. Soc.*, **141**, 16569 (2019).
17. A. K. Inge, M. Koppen, J. Su, M. Feyand, H. Xu, X. Zou, M. O'Keeffe and N. Stock, *J. Am. Chem. Soc.*, **138**, 1970 (2016).
18. H. Tianou, W. Wang, X. Yang, Z. Cao, Q. Kuang, Z. Wang, Z. Shan, M. Jin and Y. Yin, *Nat. Commun.*, **8**, 1261 (2017).
19. L. Q. Ye, L. J. Wang, H. Q. Xie, Y. R. Su, X. L. Jin and C. Zhang, *Energy Technol.*, **3**, 1115 (2015).
20. H. Y. Xu, X. Han, Q. Tan, K. J. Wu and S. Y. Qi, *Front. Mater. Sci.*, **11**, 120 (2017).
21. J. H. Hou, D. Dai, R. Wei, X. G. Wu, X. Z. Wang, M. Tahir and J. J. Zou, *ACS Sustain. Chem. Eng.*, **7**, 16569 (2019).
22. X. Z. Zhao, Y. G. Xia, H. P. Li, X. Wang, J. Wei, X. L. Jiao and D. R. Chen, *Appl. Catal. B-Environ.*, **297**, 120426 (2021).
23. X. Zhang, Y. Zhang, Z. Y. Feng, J. M. Zhao, Z. M. Yang, X. Wang and W. S. Wang, *Chem. Eng. J.*, **428**, 131235 (2022).
24. J. L. Li, B. X. Li, G. Z. Sui, L. J. Du, Y. Zhuang, Y. L. Zhang and Y. F. Zou, *J. Mol. Struct.*, **1231**, 130023 (2021).
25. K. Zhang, Z. W. Xu, J. L. Zhao, H. Wang, J. M. Hao, S. N. Zhang, H. J. Cheng and B. Dong, *J. Alloys Compd.*, **881**, 160665 (2021).
26. J. L. Li, Y. Zhuang, G. Z. Sui, D. X. Guo, Y. L. Zhang, Z. Luo, R. P. Xu, S. Liang and H. Yao, *Ionics*, **27**, 3185 (2021).
27. N. Zhang, L. G. Li, Q. Shao, T. Zhu, X. Q. Huang and X. H. Xiao, *ACS Appl. Energ. Mater.*, **2**, 8394 (2019).
28. X. Q. Zheng, L. P. Feng, Y. W. Dou, H. T. Guo, Y. C. Liang, G. Q. Li, J. J. He, P. F. Liu and J. He, *ACS Nano*, **15**, 13209 (2021).
29. X. J. Ren, M. C. Gao, Y. F. Zhang, Z. Z. Zhang, X. Z. Cao, B. Y. Wang and X. X. Wang, *Appl. Catal. B-Environ.*, **274**, 119063 (2020).
30. H. Q. Shi, X. W. Wei, J. Zhang, Q. Long, W. J. Liu, Y. M. Zhou and Y. Ding, *ChemistrSselect*, **5**, 6230 (2020).
31. X. J. Wang, X. N. Xu, Y. J. Han and X. N. Chen, *Cryst. Res. Technol.*, **50**, 405 (2015).
32. P. F. Zhou, Y. B. Shen, S. K. Zhao, G. D. Li, B. Y. Cui, D. Z. Wei and Y. S. Shen, *Chem. Eng. J.*, **407**, 126697 (2021).
33. C. Song, L. J. Wang, S. M. Sun, Y. Wu, L. J. Xu and L. Gan, *New Carbon Mater.*, **35**, 609 (2020).
34. F. D. Gao, D. W. Zeng, Q. W. Huang, S. Q. Tian and C. S. Xie, *Phys. Chem. Chem. Phys.*, **14**, 10572 (2012).
35. S. M. Fu, G. S. Li, X. Wen, C. M. Fan, J. X. Liu, X. C. Zhang and R. Li, *T. Nonferr. Metal. Soc.*, **30**, 765 (2020).
36. W. J. Liu, S. Wang, Y. Zhao, C. X. Sun, H. T. Xu and J. Z. Zhao, *J. Alloy. Compd.*, **861**, 157995 (2021).
37. J. L. Li, T. Liu, G. Z. Sui and D. S. Zhen, *J. Nanosci. Nanotech.*, **15**, 1408 (2015).
38. M. C. Gao, D. F. Zhang, X. P. Pu, X. Shao, H. Li, D. D. Lv and R. J. Xie, *J. Am. Chem. Soc.*, **99**, 881 (2015).
39. J. Song, X. Q. Wang, J. H. Yan, J. Y. Yu, G. Sun and B. Ding, *Sci. Rep.*, **7**, 1636 (2021).
40. W. Liu, Q. Yang, Z. Wang, X. F. Lv and Z. L. Yang, *Appl. Organomet. Chem.*, **32**, 4354 (2018).
41. G. Z. Sui, J. L. Li, T. Liu, T. T. Zhao, Z. L. Hao, D. S. Zhen, J. Lv, L. H. Jia and T. Jing, *Mater. Express*, **6**, 1 (2016).
42. C. Wang, G. Z. Sui, D. X. Guo, J. L. Li, L. Zhang, S. B. Li, J. J. Xin, D. F. Chai and W. X. Guo, *J. Colloid Interface Sci.*, **599**, 577 (2021).
43. J. L. Li, D. S. Zhen, G. Z. Sui, C. M. Zhang, Q. G. Deng and L. H. Jia, *J. Nanosci. Nanotech.*, **12**, 6265 (2012).
44. H. L. Tian, Y. Gu, H. L. Zhou, Y. P. Huang, Y. F. Fang, R. P. Li and C. C. Tang, *Mat. Sci. Eng. B-Adv.*, **271**, 115297 (2021).
45. X. Zhang, L. W. Wang, C. Y. Wang, W. K. Wang, Y. L. Chen, Y. X. Huang, W. W. Li, Y. J. Feng and H. Q. Yu, *Chem-Eur. J.*, **21**, 11872 (2015).
46. G. H. Dong, K. Lang, Y. Y. X. Gao, W. Z. Zhang, D. X. Guo, J. L. Li, D. F. Chai, L. Q. Jing, Z. H. Zhang and Y. Y. Wang, *J. Collid Interface Sci.*, **608**, 2921 (2022).
47. G. Z. Sui, Y. L. Zhang, J. L. Li, Y. Zhuang, D. X. Guo, Z. Luo, R. P. Xu, S. Liang, H. Yao and C. Wang, *Korean J. Chem. Eng.*, In press (2022).
48. R. P. Xu, J. L. Li, G. Z. Sui, Y. Zhuang, D. X. Guo, Z. Luo, S. Liang, H. Yao, C. Wang and S. J. Chen, *Appl. Surf. Sci.*, **578**, 152064 (2022).
49. J. Pan, S. B. Li, F. B. Li, W. Z. Zhang, D. X. Guo, L. Zhang, D. Q. Zhang, H. Pan, Y. S. Zhang and Y. F. Ruan, *J. Alloy. Compd.*, **890**, 161781 (2022).
50. Y. P. Zhang, P. Y. Cao, X. H. Zhu, B. Z. Li, Y. F. He, P. F. Song and R. M. Wang, *J. Environ. Manage.*, **299**, 113636 (2021).
51. J. L. Li, S. Q. Jia, G. Z. Sui and L. J. Du, *Chem. Pap.*, **72**, 369 (2018).